



HAL
open science

Measuring the fine-structure constant on a white dwarf surface; a detailed analysis of Fe v absorption in G191–B2B

J. Hu, J.K. Webb, T.R. Ayres, M.B. Bainbridge, J.D. Barrow, M.A. Barstow, J.C. Berengut, R.F. Carswell, V. Dumont, V. Dzuba, et al.

► **To cite this version:**

J. Hu, J.K. Webb, T.R. Ayres, M.B. Bainbridge, J.D. Barrow, et al.. Measuring the fine-structure constant on a white dwarf surface; a detailed analysis of Fe v absorption in G191–B2B. *Monthly Notices of the Royal Astronomical Society*, 2021, 500 (1), pp.1466-1475. 10.1093/mnras/staa3066 . hal-02934078

HAL Id: hal-02934078

<https://hal.science/hal-02934078>

Submitted on 24 May 2024

HAL is a multi-disciplinary open access archive for the deposit and dissemination of scientific research documents, whether they are published or not. The documents may come from teaching and research institutions in France or abroad, or from public or private research centers.

L'archive ouverte pluridisciplinaire **HAL**, est destinée au dépôt et à la diffusion de documents scientifiques de niveau recherche, publiés ou non, émanant des établissements d'enseignement et de recherche français ou étrangers, des laboratoires publics ou privés.

Measuring the fine-structure constant on a white dwarf surface; a detailed analysis of Fe V absorption in G191–B2B

J. Hu,¹ J. K. Webb^{1b},^{2★} T. R. Ayres,³ M. B. Bainbridge,⁴ J. D. Barrow,⁵ M. A. Barstow,⁴ J. C. Berengut,² R. F. Carswell^{1b},⁶ V. Dumont^{1b},⁷ V. Dzuba,² V. V. Flambaum,² C. C. Lee,⁵ N. Reindl,⁸ S. P. Preval^{1b}⁴ and W.-Ü L. Tchang-Brillet⁹

¹ADACS, Swinburne University of Technology, Hawthorn, VIC 3122, Australia

²School of Physics, University of New South Wales, Sydney, NSW 2052, Australia

³Center for Astrophysics and Space Astronomy, University of Colorado, 389 UCB, Boulder, CO 80309-0389, USA

⁴Department of Physics and Astronomy, University of Leicester, University Road, Leicester LE1 7RH, UK

⁵DAMTP, Centre for Mathematical Sciences, University of Cambridge, Cambridge CB3 0WA, UK

⁶Institute of Astronomy, Madingley Road, Cambridge CB3 0HA, UK

⁷Computational Research Division, Lawrence Berkeley National Laboratory, Berkeley, CA 94720, USA

⁸Institute for Physics and Astronomy, University of Potsdam, Karl-Liebknecht-Str. 24/25, D-14476 Potsdam, Germany

⁹LERMA, Observatoire de Paris-Meudon, PSL Research University, CNRS UMR8112, Sorbonne Université, F-92195 Meudon, France

Accepted 2020 September 24. Received 2020 September 24; in original form 2020 July 23

ABSTRACT

The gravitational potential $\phi = GM/Rc^2$ at the surface of the white dwarf G191–B2B is 10 000 times stronger than that at the Earth’s surface. Numerous photospheric absorption features are detected, making this a suitable environment to test theories in which the fundamental constants depend on gravity. We have measured the fine-structure constant, α , at the white dwarf surface, used a newly calibrated *Hubble Space Telescope* (*HST*) Space Telescope Imaging Spectrograph spectrum of G191–B2B, two new independent sets of laboratory Fe V wavelengths, and new atomic calculations of the sensitivity parameters that quantify Fe V wavelength dependency on α . The two results obtained are: $\Delta\alpha/\alpha_0 = (6.36 \pm 0.35_{\text{stat}} \pm 1.84_{\text{sys}}) \times 10^{-5}$ and $\Delta\alpha/\alpha_0 = (4.21 \pm 0.48_{\text{stat}} \pm 2.25_{\text{sys}}) \times 10^{-5}$. The measurements hint that the fine-structure constant increases slightly in the presence of strong gravitational fields. A comprehensive search for systematic errors is summarized, including possible effects from line misidentifications, line blending, stratification of the white dwarf atmosphere, the quadratic Zeeman effect and electric field effects, photospheric velocity flows, long-range wavelength distortions in the *HST* spectrum, and variations in the relative Fe isotopic abundances. None fully account for the observed deviation but the systematic uncertainties are heavily dominated by laboratory wavelength measurement precision.

Key words: white dwarfs – cosmological parameters.

1 INTRODUCTION

General relativity (GR) has passed all weak-field observational and experimental tests to date. Nevertheless, the theory predicts singularities on small scales and is incompatible with quantum field theory. To be compatible with cosmological observations, the theory also requires most of the energy content of the universe to be in the form of an unknown dark energy. These things lead us to expect that GR will ultimately become the low-energy limit of some future more fundamental unification theory. Searches for departures from standard GR, particularly in stronger field situations, are important in this respect. This is the aim of the work described in this paper.

Fundamental constants may vary in the presence of strong gravitational fields, a possibility first proposed by Dicke (1959, 1964), the latter republished in Dicke (2019), with a related discussion given in Bekenstein (1982). More recent ideas concerning quantum gravity unification theories allow the possibility of space and time

variations in the low-energy ‘constants’ of nature, either because of the presence of extra space dimensions or the non-uniqueness of the quantum vacuum state for the universe, for example, Uzan (2011). Strong-field tests using pulsar timing observations in a triple stellar system place tight constraints on departures from standard GR (Archibald et al. 2018; Voisin et al. 2020).

Since the gravitational potential at the surface of a white dwarf is typically 4–5 orders of magnitude stronger than on Earth, white dwarf atmospheres provide an interesting environment to search for new physics or new tests of the weak equivalence principle. Discussions concerning relativistic effects in white dwarfs include Wheeler, Hansen & Cox (1968), Jain, Kouvaris & Nielsen (2016), and Carvalho, Marinho & Malheiro (2018). If relativistic effects are weak (as is the case for white dwarf surfaces; $GM/Rc^2 \sim 10^{-4}$, within an order of magnitude of the gravitational potential perturbation observed on the last scattering surface of the microwave background), the total scalar charge is proportional to the number of nucleons in the object (Flambaum & Shuryak 2008).

Near massive gravitating bodies, different types of couplings between scalar fields and other fields can lead to an increase or

* E-mail: jkw@phys.unsw.edu.au

decrease in the coupling constant strengths (Magueijo, Barrow & Sandvik 2002). These scalar fields can be the carriers of variations in traditional constants of physics, like G , α , and m_e/m_p and so precision studies of white dwarf atmospheres offers a new laboratory for fundamental physics that is not available on Earth. For small variations, the scalar field variation is proportional to the change in the dimensionless gravitational potential, $\phi = GM/Rc^2$ and hence to the compactness (M/R) of an object. Compact objects with high mass and small radius, could thus exhibit variations in the fine-structure ‘constant’, α , for example, with a relative change given by

$$\frac{\Delta\alpha}{\alpha_0} = \frac{\alpha_\phi - \alpha_0}{\alpha_0} \propto \Delta\phi, \quad (1)$$

where $\Delta\phi$ is a change in the gravitational potential (in this case the difference between the white dwarf and terrestrial values). Inhomogeneous variations in the cosmological setting were studied in Barrow, Magueijo & Sandvik (2002), Mota & Barrow (2004a, b), and Barrow & Mota (2003).

Few observational constraints exist. The first was reported in Berengut et al. (2013) who measured $\Delta\alpha/\alpha_0$ on the surface of the white dwarf G191–B2B for which $\log(\phi) = -4.3$. Recently, Hees et al. (2020) measured $\Delta\alpha/\alpha_0$ in five stars in the vicinity of the Galactic centre, at a distance from the supermassive black hole ($4.6 \times 10^6 M_\odot$) such that $\log(\phi) = -5.6$, that is, at a gravitational potential ~ 20 times smaller than the surface of G191–B2B, with a claimed constraint $\Delta\alpha/\alpha_0 < 10^{-5}$.

In this paper, we present a detailed analysis of the spectrum of G191–B2B to measure $\Delta\alpha/\alpha_0$. We make use of the *many-multiplet method* (Dzuba, Flambaum & Webb 1999b; Webb et al. 1999; Dzuba, Flambaum & Marchenko 2003; Flambaum & Dzuba 2009), as did Berengut et al. (2013). A new analysis of G191–B2B is required because: (i) two new samples of Fe V laboratory wavelength measurements have since been published, (ii) the G191–B2B *Hubble Space Telescope (HST)* Space Telescope Imaging Spectrograph (STIS) spectra themselves have been refined/re-reduced, in principle providing a more accurate calibration, (iii) the Berengut et al. (2013) analysis used simple line centroid measurements, which do not readily identify line blends or other anomalies. Here, we use a different approach – simultaneously fitting many Fe V transitions using Voigt profiles (which effectively means that we model the data using far fewer positional parameters), and (iv) the coefficients used to parametrize each transition’s sensitivity to a change in α have been independently re-calculated (Section 4.3).

The structure of the remainder of this paper is as follows: Section 2 provides a brief reminder of basic white dwarf astrophysics and describes previous constraints. Section 3 describes the *HST/STIS* spectra of the white dwarf G191–B2B. Section 4 details all atomic/laboratory data used. Section 5 discusses line detection in the G191–B2B spectrum, matching those lines with the laboratory Fe V wavelengths, and the further refinement of the sample to remove weak and asymmetric features. Section 6 presents the modelling procedures for measuring $\Delta\alpha/\alpha_0$ and Section 7 summarizes the results of numerical calculations quantifying several possible sources of systematic error. Sections 8 and 9 present and discuss the final results.

2 OBSERVATIONAL CONSTRAINTS USING WHITE DWARFS

White dwarfs are the most common end-products of stars. More than 95 per cent of stars in our Galaxy will end up as white dwarfs. Stars with initial masses of $\sim (1-8) M_\odot$ eventually evolve into white

dwarfs (Fontaine et al. 2013). As stars evolve, the energy generated by nuclear interactions fails to balance gravity and collapse occurs. Stable radii are reached when electron degeneracy pressure balances gravity (Koester & Chanmugam 1990), leaving very compact, high surface gravity remnants, white dwarfs. A typical white dwarf has an oxygen/carbon core surrounded by a thin hydrogen/helium (H/He) envelope. Due to processes such as levitation (Chayer, Fontaine & Wesemael 1995) and debris accretion from disrupted planetary systems, interstellar material, or comets (Zuckerman et al. 2003), metallic elements are found in the atmosphere.

White dwarfs are classified according to spectral features (e.g. atmospheric composition and colour), DA white dwarfs being those with a hydrogen enriched atmosphere (Sion et al. 1983). These white dwarfs are useful test beds for investigating dependence of fine-structure constant variation on strong gravitational field. Some non-DA white dwarfs that have similar characteristics can also be used, such as the hot subdwarf O star, BD+28°4211. White dwarf characteristics that are desirable for α measurements include (i) a strong surface gravitational field; DA white dwarfs can have surface gravity $\log g$ between ~ 7 and ~ 8 (Bergeron, Saffer & Liebert 1992), and (ii) multiple heavy element transitions; various species, including Fe V or Ni V have been observed in white dwarf spectra (Sion et al. 1992; Holberg et al. 1994; Werner & Dreizler 1994). These highly ionized lines are particularly useful for measuring variation in fine-structure constant (α), as they are very sensitive to a change in α .

Hot DA white dwarfs with metal lines typically have effective temperatures $T_{\text{eff}} \geq 50\,000$ K (Barstow et al. 2003, 2014). The STIS provides the highest resolution available for ultraviolet (UV) spectroscopy, the E140H grating having a resolving power of 114 000. Detailed analyses of the white dwarf G191–B2B are reported in Preval et al. (2013) and Rauch et al. (2013). By comparing the observed data with non-local thermodynamic equilibrium model spectra, many Fe V and Ni V absorption features were identified.

The first astronomical measurement of α variation in strong gravitational fields (Berengut et al. 2013) used the Preval et al. (2013) spectrum and line identifications. Applying the many-multiplet method (Dzuba et al. 1999b; Webb et al. 1999), two $\Delta\alpha/\alpha_0$ measurements using Fe V and Ni V lines separately gave $\Delta\alpha/\alpha_0(\text{Fe V}) = (4.2 \pm 1.6) \times 10^{-5}$, and $\Delta\alpha/\alpha_0(\text{Ni V}) = (-6.1 \pm 5.8) \times 10^{-5}$. The discrepancy between these two measurements suggested significant laboratory wavelength systematics in either the Fe V or the Ni V line lists, or both.

Analyses of additional spectra are described in Bainbridge et al. (2017a, b), who discuss the possibility of making $\Delta\alpha/\alpha_0$ measurements over a wide range in surface gravity using eight white dwarfs, including G191–B2B. Collectively, the eight results based on Fe V hint at a non-zero (positive) $\Delta\alpha/\alpha_0$ and a possible correlation with field strength. However, since those measurements are highly preliminary and include no estimate of systematics, we defer any further quantitative comments regarding those spectra to a later paper.

3 ASTRONOMICAL DATA

The analysis described in this paper is based on a high signal-to-noise STIS FUV spectrum of the white dwarf G191–B2B. The observations, data reduction, and other details are described fully in Hu et al. (2019), so only a brief summary is given here. G191–B2B is a common calibration source for STIS so the total integration time is high. In total, 37 archival E140H exposures of G191–B2B using the 0.2×0.2 arcsec aperture were used. The E140H observations were conducted between 1998 and 2009 in observing cycles 7, 8, 10, and 17. The total E140H exposure time is 17.36 h. In addition

Table 1. Summary of atomic data. **K14** are Ritz wavelengths (Kramida 2014). Lines that we used for measuring $\Delta\alpha/\alpha_0$ are marked with a \star . The bulk of the analysis described in this paper was carried out on a pre-publication version of the **W19** tabulated Fe V lines that had been assigned different uncertainty estimates. The initial cut (accepting only lines with uncertainties ≤ 4 mÅ), and the subsequent filtering, results in our final **W19** sample being those lines marked in this table with a \diamond . The pre-publication Fe V tabulation has not been given here – in this table we list the **W19** data as published in Ward et al. (2019). Columns 2–4 and 5–7 are the lower and upper level configuration, term, and J values, adopted from table 1 in Kramida (2014) and from NIST (https://physics.nist.gov/PhysRefData/ASD/lines_form.html). Columns 8 and 9 are the lower and upper energy levels. Oscillator strength f are from Kramida (2014) if available. 18 lines with missing values are supplemented by data from the Kurucz data base (\dagger). Γ values are taken from Aggarwal et al. (2017) where available. 15 lines with missing values are supplemented by data from Kurucz data base (marked with a \S). The q -coefficients given in this table are new calculations and supersede those of Ong et al. (2013). This table only shows 10 entries. The full table is provided as Supporting Information.

ID	C1	T1	J1	C2	T2	J2	E1 (cm ⁻¹)	E2 (cm ⁻¹)	K14		W19		f	Γ (s ⁻¹)	q (cm ⁻¹)
									λ (Å)	$\delta\lambda$ (Å)	λ (Å)	$\delta\lambda$ (Å)			
60	3d3.(2D1).4s	3D	1	3d3.(2D1).4p	3P*	1	258769.6	335267.9	1307.2190	0.0030	1307.2216	0.0024	9.6e-02	4.17E+09	2862
61	3d3.(2P).4s	1P	1	3d3.(2P).4p	1P*	1	219486.7	295973.0	1307.4242	\star 0.0023	1307.4237	\diamond 0.0024	2.2e-01	6.80E+09	2311
62	3d3.(2G).4s	3G	4	3d3.(2P).4p	3D*	3	209109.9	285474.0	1309.5147	0.0020			1.1e-02	5.65E+09	2992
63	3d3.(2P).4s	3P	1	3d3.(2D2).4p	3P*	0	214611.3	290903.4	1310.7510	0.0030			6.0e-04	8.06E+09	3286
64	3d3.(4P).4s	3P	2	3d3.(2D2).4p	3D*	3	213649.0	289912.8	1311.2378	0.0019	1311.2293	0.0074	3.8e-02	5.88E+09	2389
65	3d3.(2P).4s	1P	1	3d3.(2D2).4p	1D*	2	219486.7	295716.2	1311.8290	\star 0.0030	1311.8278	\diamond 0.0024	1.9e-01	1.01E+10	1616
66	3d3.(4P).4s	3P	0	3d3.(2D2).4p	3D*	1	212542.0	288669.5	1313.5851	\star 0.0023			6.6e-02	6.17E+09	2507
67	3d3.(2G).4s	3G	3	3d3.(2P).4p	3D*	2	208838.0	284911.0	1314.5256	\star 0.0017	1314.5292	\diamond 0.0026	2.2e-03	5.21E+09	2920
68	3d3.(2D1).4s	3D	2	3d3.(2D1).4p	3P*	2	258628.6	334509.2	1317.8610	0.0030	1317.8611	0.0024	7.0e-02	4.20E+09	
69	3d3.(2G).4s	3G	3	3d3.(2H).4p	3H*	4	208838.0	284690.3	1318.3505	0.0021	1318.3488	0.0024	6.0e-02	5.99E+09	3660

to the E140H exposures, which cover the wavelength range (1150–1700) Å. There are also five exposures taken between 2000 and 2009 in observing cycles 9, 10, and 17, using the shortest wavelength setting (1763 Å) with the E230H grating covering the range (1630–1897) Å. The full coverage of the spectrum spans 1150–1897 Å. The spectral resolution is $\lambda/\Delta\lambda \approx 114\,000$.

4 ATOMIC DATA

4.1 Laboratory and Ritz wavelengths

The analysis of G191–B2B by Berengut et al. (2013) showed that wavelength errors dominate the $\Delta\alpha/\alpha_0$ uncertainty. That analysis used the best available wavelengths at that time (Ekberg 1975). Two more new Fe V wavelength data sets have been published since then: the Ritz calculations of Kramida (2014), and the laboratory measurements by Ward et al. (2019) at National Institute of Standards and Technology. For the measurement of $\Delta\alpha/\alpha_0$ presented in this paper, we used the Fe V electric dipole (E1) transitions available from these two new wavelength data sets (the majority being $3d^34s$ – $3d^34p$ transitions) that lie in the range 1149–1705 Å. We now comment briefly on each set of Fe V laboratory wavelengths used in our analysis.

4.1.1 Kramida 2014 (hereafter, K14)

This set of Fe V lines is from Kramida (2014). He used previous laboratory measurements of around 2000 wavelengths, including Ekberg (1975), Azarov et al. (2001), Fawcett & Henrichs (1974), and Kalinin et al. (1985), with the lines in the wavelength range of interest to this study being dominated by the measurements of Ekberg (1975). Kramida (2014) applied a least-squares fitting method (Kramida 2011) to determine optimized energy levels and hence Ritz wavelengths. Since multiple spectral lines are used to determine the energy levels, Ritz wavelengths generally have smaller uncertainties than individual laboratory experiment sets. However, this also means that wavelength calibration errors affect the Ritz wavelengths in a complex way as they are determined from spectral lines in different wavelength regions. Within our wavelength range of interest, the uncertainties lie in the range is 1.5–8 mÅ.

4.1.2 Ward et al 2019 (hereafter, W19)

This set of Fe V lines comes from an experiment to measure Fe V and other species at the NIST, Gaithersburg, Maryland, USA (Ward & Nave 2015a, b; Ward et al. 2019). The experiment measured 164 Fe V lines between 1200 and 1600 Å. In this sample, uncertainties are assigned to each Fe V wavelength and lie in the range 2.4–10 mÅ.

We opt to remove the least accurate Fe V wavelengths from both samples. For **K14** we discard all lines with uncertainties greater than 4 mÅ. The 4 mÅ cut is mildly arbitrary but was chosen because it is the measurement uncertainty for the Fe V sample from Ekberg (1975) on which the optimized **K14** sample is based and in order retain a significant number lines in the sample. This leaves 377 lines. For **W19**, we do the same (but see the caption to Table 1). This leaves 129 lines.

To examine consistency, in Fig. 1 we plot wavelength difference for pairs of lines from the two wavelength data sets. $\Delta\lambda$, the difference between **W19** and **K14** wavelength, has a mean value of 0.2 mÅ, with a standard deviation of 3.7 mÅ.

4.2 Other atomic data

Since we are fitting Voigt profiles to the observed Fe V absorption lines in the G191–B2B atmosphere, the column density parameter returned from the Voigt profile fitting is only a measure of line strength (and does not give a true column density estimate). To calculate Voigt profile models, we necessarily require values for the oscillator strength f and damping constant Γ . The f values are taken from Kramida (2014), supplemented by 18 missing values from the Kurucz data base.¹ Γ values are taken from Aggarwal et al. (2017) where available and Kurucz’s values used otherwise. However, in our modelling procedure, each observed transition is assigned its own column density and velocity dispersion parameter (b -parameter). Only relative line positions are tied in the fitting procedure. This means that the oscillator strengths and damping coefficients are effectively treated as free parameters.

¹<http://kurucz.harvard.edu/>

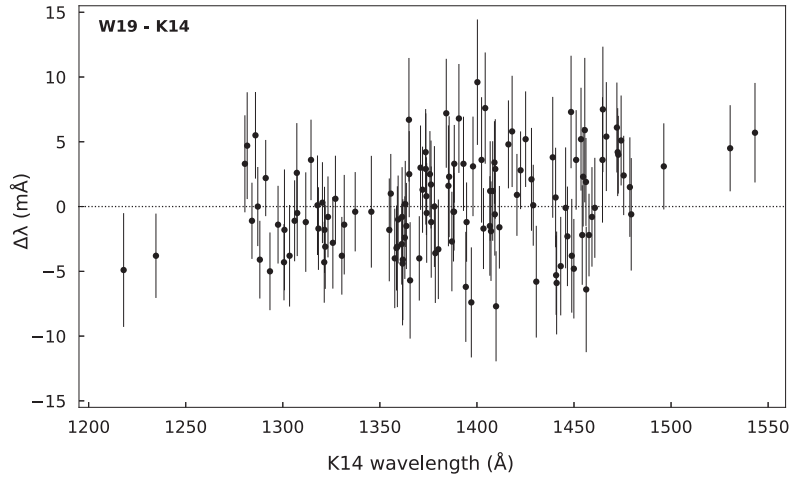


Figure 1. The difference between the W19 and K14 wavelengths. See Ward et al. (2019) for a detailed comparison between Fe V wavelength sets.

4.3 Sensitivity coefficient calculations

The wavenumber ω of a transition measured in the white dwarf rest frame is given by

$$\omega = \omega_0 + qx, \quad (2)$$

where ω_0 is the laboratory wavenumber, q is the sensitivity coefficient to changes in α , and $x = (\alpha_\phi/\alpha_0)^2 - 1$ (Dzuba, Flambaum & Webb 1999a; Webb et al. 1999).

New Fe V q -coefficients for transitions involving $3d^34s$ and $3d^34p$ configurations have been calculated. The same approach as in Ong, Berengut & Flambaum (2013) has been followed, but the new calculations include about a hundred new states, leading to an enormous number of new electric dipole transitions. The calculations use the combined configuration interaction and the many body perturbation theory method, CI+MBPT (Dzuba, Flambaum & Kozlov 1996; Dzuba & Johnson 1998). The B-spline technique (Johnson & Sapirstein 1986) is used to construct a single-electron basis set. The calculations are done in the V^{N-4} approximation (Dzuba 2005), which means that the initial self-consistent Hartree–Fock procedure is done for the closed-shell Ar-like Fe IX ion with all four valence electrons removed. The basis states in valence space are calculated in the frozen field of the Ar-like Fe IX core. The CI technique is used to construct four-electron valence states, while MBPT is used to include core–valence correlations (see Ong et al. (2013), Dzuba et al. (1996), Dzuba & Johnson (1998) for further details).

An analysis of the accuracy of the calculations is described in Ong et al. (2013). This includes calculations with different initial approximations (V^N , V^{N-1} , etc.) which give very close results. Therefore, in this paper, we use just one approach based on the V^{N-4} potential. It is slightly different from the methods used in Ong et al. (2013) and independent computer codes were used. Comparing the two sets of coefficients therefore provides an empirical estimate of the q -coefficient uncertainties. In the end, we believe that the q -coefficient uncertainty does not exceed 10 per cent. For Fe V lines to be used in measuring $\Delta\alpha/\alpha_0$, we must of course have q -coefficients; 345 of the 377 in the K14 sample and 120 of the 129 in the W19 sample have these.

Inspection of Table 1 shows that some transitions have not been assigned q -coefficients. The reason for this is that due to the high density of excited states, matching the observed and calculated energy levels is sometimes ambiguous. This means we cannot

reliably assign q -coefficients to some of the observed transitions. Therefore, we have not presented values of q in some cases. We noted (subsequent to the completion of this work) that matching energy levels can be clarified using the procedures of Kramida (2013). This is a possible area to be developed in future work so that more transitions can be used.

5 LINE DETECTION, IDENTIFICATION, AND SAMPLE REFINEMENT

5.1 5σ detections using RDGEN

RDGEN is a multipurpose program for spectroscopic data analysis (Carswell et al. 2014). One useful function is the detection of absorption lines above a given statistical significance, relative to a user-supplied continuum level. A reliable spectral variance array is required. The algorithm uses the known spectral resolution to constrain the minimum separation between adjacent or blended features. It returns line centroids, equivalent widths, and other relevant measurements, with associated error estimates. Our first step is to measure lines in the G191–B2B spectrum above a 5σ detection threshold.

5.2 Matching the detected and laboratory wavelengths

The laboratory wavelength sets are derived from terrestrial experiments for which $\Delta\alpha/\alpha_0 = 0$. The number of absorption lines per unit wavelength interval in the spectrum of G191–B2B is reasonably high, so it may be possible to wrongly associate observed and laboratory lines if the tolerance is insufficiently stringent and/or if in fact $\Delta\alpha/\alpha_0 \neq 0$ near a white dwarf. If $\Delta\alpha/\alpha_0 \neq 0$ near a white dwarf, making the assumption that $\Delta\alpha/\alpha_0 = 0$ may result in line misidentifications (and bias a $\Delta\alpha/\alpha_0$ measurement towards zero). Since we do not know a priori the value of $\Delta\alpha/\alpha_0$ at the white dwarf atmosphere, it is therefore preferable to avoid making any assumption about $\Delta\alpha/\alpha_0$ when identifying the observed G191–B2B absorption lines. To avoid this problem, line identification is carried out as a function of $\Delta\alpha/\alpha_0$, over the range $-10^{-3} < \Delta\alpha/\alpha_0 < 10^{-3}$, in steps of 10^{-5} . The K14 wavelengths have the largest number of lines available (345 lines) so this data set was used for line identification.

The G191–B2B redshift used is obtained from the measured value of $v = 23.8 \pm 0.03$ km s $^{-1}$ (Preval et al. 2013), obtained using

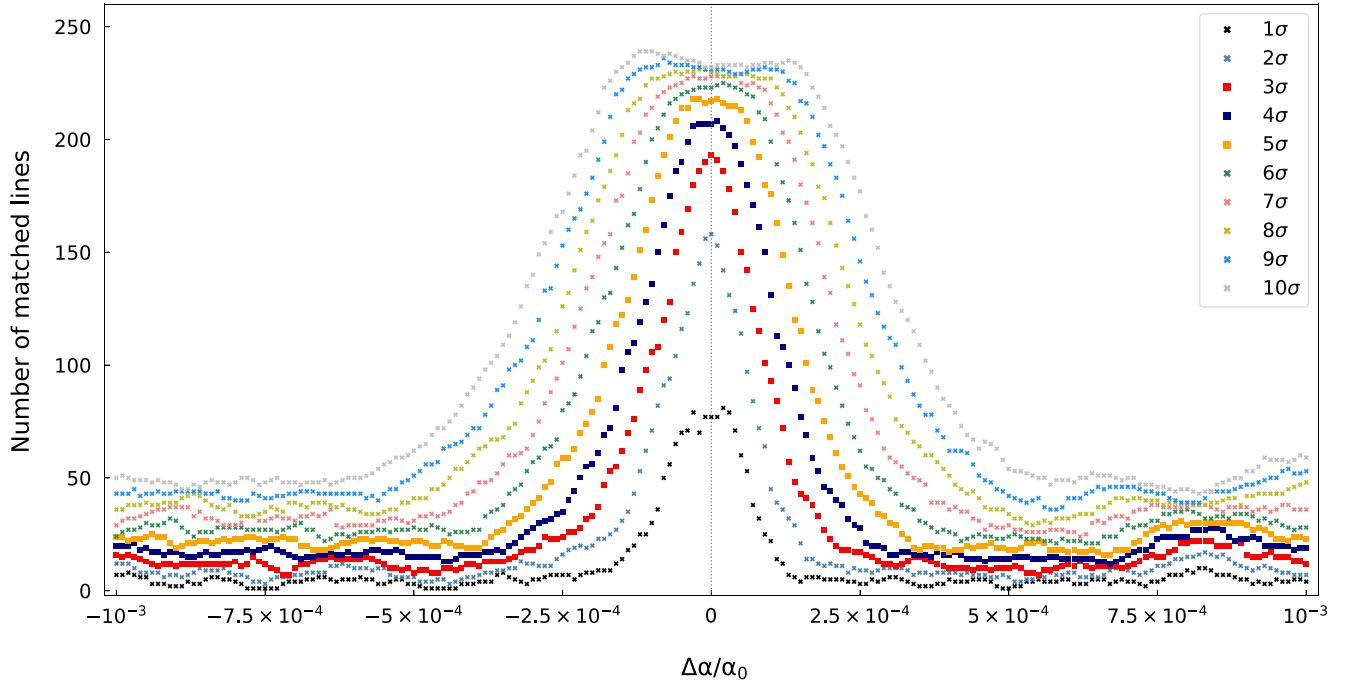


Figure 2. This figure illustrates the identification Fe V lines in the spectrum of G191–B2B without assuming that $\Delta\alpha/\alpha = 0$, avoiding measurement bias. Lines are identified by stepping through $-10^{-3} < \Delta\alpha/\alpha < 10^{-3}$ in steps of 10^{-5} , modifying the Fe V laboratory wavelengths according to equation (3), then matching laboratory and rest-frame wavelengths using the tolerance defined by equation (5). Each coloured curve corresponds to a different tolerance ($n = 1, 2, 3, \dots, 10$) for colours blue, green, grey, . . . , red. As the identification criterion is relaxed, more lines are identified and the curves become increasingly flat-topped, as expected.

the weighted average of all the identified atmospheric lines (i.e. all identified species, not just Fe V).

Re-arranging equation (2) and using $\omega = \omega'(1 + z)$, the observed-frame laboratory wavelength becomes

$$\lambda' = \frac{\lambda_0(1 + z)}{1 + qx/\omega_0} \quad (3)$$

$$\approx \lambda_0(1 + z) \left(1 - \frac{Q\Delta\alpha}{\alpha_0} \right), \quad (4)$$

where ω' is the observed-frame wavenumber, z is its redshift (the summed effects of stellar peculiar velocity and gravitational redshift), λ_0 is the terrestrial laboratory wavelength, the dimensionless quantity $Q = 2q/\omega_0$, $x \approx 2\Delta\alpha/\alpha_0$, and where the first two Taylor-series terms have been used to approximate the factor of $1/(1 + qx/\omega_0)$ in equation (3).

For a line to be identified as Fe V, we require the observed and laboratory wavelengths to agree within

$$\Delta\lambda = |\lambda_{\text{obs}} - \lambda'| \lesssim n\sqrt{\sigma(\lambda_{\text{obs}})^2 + \sigma(\lambda')^2}, \quad (5)$$

where λ_{obs} and λ' are the observed-frame white dwarf and laboratory wavelengths. The error contribution due to the white dwarf redshift is small compared to the other terms so has been ignored.

The results of these calculations for a range of n are illustrated in Fig. 2. As can be seen, line identification maximizes at or very close to $\Delta\alpha/\alpha_0 = 0$. The plateauing at large n occurs because the generous identification criterion results in many accepted identifications for each line. The final tolerance used to select lines is $n = 3$. This procedure serves two purposes: first, it indicates that if $\Delta\alpha/\alpha_0$ does depart from zero, it is only by a small amount. Second, it suggests that even if we identify lines using $\Delta\alpha/\alpha_0 = 0$ with a 3σ tolerance, we are unlikely to bias the final result much.

5.3 Removing blended and weak lines

The total number of Fe V absorption lines detected in the G191–B2B spectrum using the above selection parameters was 199. We now refine this list by removing blended features. Where RDGEN detects multiple components in an absorption feature in the observed G191–B2B spectrum and where one of the detected components is Fe V and the other, or others, are not identified as Fe V, that whole absorption feature is discarded. This reduces the total number identified of Fe V lines to 164.

Another means of identifying blended profiles comes from the laboratory measurements. The K14 Fe V list identifies eight cases where a line is resolved into two components on the basis of energy level calculations. These eight lines are discarded, reducing the total number of identified Fe V lines to 148.

All remaining lines are fitted with Voigt profiles (convolved with the appropriate line spread function, lsf – see Section 6 for details). All line parameters are initially untied, that is, each line is fitted with three parameters, column density, velocity dispersion parameter b , and redshift. χ^2 for each fit provides a check on goodness of fit. In a few cases, a high value of χ^2 indicates a non-Voigt line shape that had not been picked up earlier. Therefore these lines are removed from the analysis, discarding all lines that returned a $\chi_n^2 > 1.5$. This cut reduces the number of lines used from the G191–B2B spectrum from 148 to 135 lines.

Although lines have been detected above 5σ , some of the detected features are weak and do not contribute significantly to the $\Delta\alpha/\alpha_0$ measurement. For this reason we apply a final cut: lines with observed equivalent widths less than 0.002 \AA (38 lines) are removed. This step reduces the number of lines used from the G191–B2B spectrum from 135 to 97. Finally, out of the 97 observed lines, all of which have K14 wavelengths, 63 also have W19 wavelengths.

An extract of the complete table of observed lines is given in Table 2. The full line list is provided as online Supporting Information.

6 MEASURING $\Delta\alpha/\alpha_0$

To solve for $\Delta\alpha/\alpha_0$, all Fe V redshift parameters are tied so that the whole sample is parametrized using one single redshift parameter. This removes 96 redshift parameters compared to the modelling described in Section 5.3. With all line redshifts tied, VPFIT is then used to solve for $\Delta\alpha/\alpha_0$. The default VPFIT set-up parameters (Carswell & Webb 2020a,b) are used with one important exception. The Isf of the spectrograph and grating (STIS with 140H) is non-Gaussian. Voigt profiles must be convolved with the appropriate Isf² during the modelling process. The non-default VPFIT set-up parameter is the number of sub-bins per pixel, which is set to 13, the number of pixels in the STIS Isf. The free parameters in the fit are thus *all* velocity dispersion parameters (one for each absorption line), *all* line strengths (‘effective column densities’, one for each absorption line), one redshift parameter z for the whole sample, and one $\Delta\alpha/\alpha_0$ parameter.

Once all redshift parameters are tied and the spectrum re-fitted, a small number of previously well-fitted lines produce high χ^2 values. Potential causes of this include:

- (i) line blending that previously went undetected, that is, an Fe V line may be correctly identified, but some other species is blended with it (the blended profile remaining reasonably symmetric and hence well fitted by a single Voigt profile in Section 5.3) causing a small shift in the observed wavelength. These would only show up once tied redshifts were introduced;
- (ii) wavelength calibration errors in the G191–B2B spectrum, although these would necessarily have to be localized, otherwise correlated groups of Fe V lines would appear discrepant and this seems not to be the case;
- (iii) uncertainties in individual Fe V laboratory wavelengths;
- (iv) incorrect q -coefficients could cause discrepant χ^2 values for individual lines (although if $\Delta\alpha/\alpha_0 = 0$, equation (2) shows these have no effect);
- (v) it is possible (although unlikely) that misidentified lines remain in the sample, i.e. lines which have up until now been assumed to be Fe V but in fact are some other species.

Regardless of their origin, these points are clipped in an iterative procedure, removing individual spectral fitting regions having normalized $\chi_n > 2$ one at a time, re-fitting for $\Delta\alpha/\alpha_0$ at each iteration. There are a few groups of lines close to each other, thus in the same fitting region. In those cases, if $\chi_n > 2$ for the region as a whole, that region is discarded.

After all selection procedures, the numbers of lines used for the two $\Delta\alpha/\alpha_0$ measurements are 92 with K14 wavelengths and 53 with W19 wavelengths. Fig. 3 shows 9 example profiles. The left hand column shows the best-fit model, $\Delta\alpha/\alpha_0 = 6.36 \times 10^{-5}$. The middle column illustrates the same model as in the left column but with $\Delta\alpha/\alpha_0$ simply reset to zero. The right hand column shows the best-fit model without $\Delta\alpha/\alpha_0$ as a free parameter i.e. it is assumed to be zero. The figure illustrates the marginally better fit obtained when $\Delta\alpha/\alpha_0$ is allowed to vary.

7 MEASUREMENT UNCERTAINTIES

Known and potential sources of error have been investigated in considerable detail. Here, we briefly described each one and list them in Table 3.

7.1 VPFIT measurement uncertainty

The VPFIT error (obtained from the covariance matrix at the best-fitting solution) depends only on the G191–B2B spectral properties and does not take into account other effects such as laboratory wavelength uncertainties. The method has been checked many times previously, for example, King et al. (2009), but even so has been carefully verified again in this context. We generated 1000 synthetic spectra based on the Fe V laboratory wavelengths and the observed G191–B2B spectral properties. Each was fitted and the (known) $\Delta\alpha/\alpha_0$ solved for. The statistical distribution from the 1000 $\Delta\alpha/\alpha_0$ estimates can then be compared to the covariance matrix error estimate. The two values agree well.

7.2 Laboratory wavelength uncertainties

In the Fe V laboratory measurements made by Ekberg (1975), the nominal line wavelength uncertainties are given as 4 mÅ. As noted in Berengut et al. (2013), directly comparing the rest-frame G191–B2B and Ekberg wavelengths suggests the actual laboratory uncertainties were somewhat smaller.

Rather than a single uncertainty estimate, both the K14 and W19 Fe V tabulations provide a range of uncertainties, depending on line quality. For K14, the range for the Fe V lines used to measure $\Delta\alpha/\alpha_0$ here is 1.5–4 mÅ. For W19, the lines used to measure $\Delta\alpha/\alpha_0$ all have a nominal uncertainty of 3 mÅ.

Additional spectral simulations were therefore also done. First, a model of the white dwarf spectrum is created using the parameters derived from fitting the real spectrum. We perturb each Fe V laboratory wavelength randomly (using the published Fe V wavelength uncertainties) and then re-fit the spectrum using the modified laboratory wavelengths to re-measure $\Delta\alpha/\alpha_0$. The procedure is repeated 10 000 times for each set of laboratory wavelengths (K14 and W19), from which we can empirically determine the scatter in $\Delta\alpha/\alpha_0$ caused by Fe V laboratory wavelength uncertainties. The results of these numerical experiments also show the nominal K14 wavelength uncertainties are overestimated although the nominal W19 uncertainties are close to correct.

7.3 Pt/Cr-Ne lamp and long-range wavelength distortion

The spectrum of G191–B2B used in this analysis is formed by combining 37 different exposures taken over an 11 year period. We do not know how stable the physical parameters of the *HST* on-board Pt/Cr-Ne emission-line calibration lamp were during time. The wavelength calibration can be also affected by (i) charge transfer inefficiency losses, (ii) instrumental changes such as thermal effects (heating and cooling of the optical bench), (iii) small variations of the position of the target along the spectrograph slit, and (iv) the *HST* orbital motion. All these factors must combine in some unknown way to produce a net wavelength calibration distortion.

Since there are no independent calibration sources for comparison, we parametrize any potential distortion using the method described in Dumont & Webb (2017). Following that procedure, we assume that the effects described above map to a linear distortion in velocity space for a single exposure. Combining multiple exposures to form a

²<http://www.stsci.edu/hst/instrumentation/stis/performance/spectral-resolution>

Table 2. Observed line wavelengths in the STIS spectrum of G191–B2B. ID refers to column 1 of Table 1. λ_{obs} is the mean observed-frame wavelength of the absorption feature with uncertainty $\sigma(\lambda_{\text{obs}})$. EW is the equivalent width with uncertainty $\sigma(\text{EW})$. The absence of $\sigma(\text{EW})$ indicates that another line is nearby such that the detection algorithm interpreted the whole feature as a blend. Wavelength and equivalent widths are in Å. Columns 6–11 give redshift z , b -parameter (in km s^{-1}) and column density $\log N$ (N is in atoms cm^{-2}) with their associated uncertainties. A tick in the last two columns indicates that a line was used for measuring α . This table only shows 10 entries. The full table is provided as Supporting Information.

ID	λ_{obs}	$\sigma(\lambda_{\text{obs}})$	EW	$\sigma(\text{EW})$	$z [\times 10^{-5}]$	$\sigma(z) [\times 10^{-5}]$	b	$\sigma(b)$	$\log N$	$\sigma(\log N)$	K14	W19
27	1250.833	0.001	0.003		7.88	0.06	4.99	0.30	12.12	0.02	✓	
36	1280.573	0.0012	0.00617	0.000197	8.17	0.04	5.36	0.18	13.22	0.01	✓	✓
38	1281.468	0.001	0.002		7.93	0.11	5.11	0.59	12.15	0.04	✓	
43	1286.015	0.001	0.002		7.73	0.06	3.68	0.30	12.51	0.02	✓	✓
45	1288.269	0.0009	0.00355	0.000148	7.89	0.04	3.98	0.20	12.73	0.01	✓	✓
48	1291.298	0.002	0.005		8.24	0.07	6.50	0.30	12.90	0.02	✓	✓
50	1293.409	0.001	0.003		7.85	0.06	5.47	0.27	13.09	0.02	✓	
51	1293.485	0.001	0.003		7.92	0.04	4.40	0.18	12.85	0.01	✓	
52	1297.651	0.001	0.005		7.95	0.04	5.13	0.17	12.91	0.01	✓	✓
53	1300.715	0.001	0.0047	0.000162	8.09	0.04	4.59	0.18	12.90	0.01	✓	

single spectrum (as we have done in this analysis) generates a more complex distortion correction function, as described in Dumont & Webb (2017). An additional free parameter (the velocity distortion slope) is included in the modelling that maps into a small shift on $\Delta\alpha/\alpha_0$ with an additional systematic error term, listed in Table 3.

7.4 Multiplet segregation

During the modelling procedure, although all line redshifts are tied such that the entire set of Fe V lines is fitted with one single redshift parameter, individual b -parameters are free. The reason for this is that there is evidence for stratification in the G191–B2B atmosphere (Barstow, Hubeny & Holberg 1999; Dreizler & Wolff 1999), which may imply that a single b value may not necessarily apply to all detected Fe V transitions. This is corroborated by a synthesized model atmosphere³ (Hubeny & Lanz 1995) for G191–B2B which predicts different atmospheric depths for different Fe V multiplets (also see Rauch et al. 2013). The computation of synthetic spectra based on TLUSTY calculations are discussed in Hubeny & Lanz (2011). Spatial segregation, in the presence of a velocity field that varies systematically with atmospheric depth, could in principle emulate varying α . Another consequence of Fe V multiplet segregation could be that different multiplets experience different gravitational redshifts. However, both of these effects have been modelled and both turn out to be very small. To illustrate this, using $\Delta z \approx GM\Delta r/r^2 c^2$, assuming a total photospheric height of 10 km, the maximum gravitational redshift difference between absorptions created at the top and bottom of the atmosphere is $\Delta z \approx 10^{-8}$. This is an order of magnitude below the *statistical* measurement uncertainty on an individual line position, thus very small compared to the net uncertainty on $\Delta\alpha/\alpha_0$.

7.5 Fe isotopic abundances

The four stable Fe isotopes have terrestrial relative abundances ⁵⁴Fe (5.845 per cent), ⁵⁶Fe (91.754 per cent), ⁵⁷Fe (2.119 per cent), and ⁵⁸Fe (0.282 per cent). Deviations from terrestrial abundances in the G191–B2B atmosphere will emulate small (energy level dependent) observed line shifts relative to a model based on terrestrial values. This may emulate a non-zero $\Delta\alpha/\alpha_0$. Variations from terrestrial isotopic abundances have been simulated by appropriately modifying

³<http://tlusty.oca.eu/>

the laboratory wavelengths and re-fitting to the G191–B2B spectrum to examine the impact on $\Delta\alpha/\alpha_0$.

7.6 Zeeman effects

If a magnetic field is present, the first-order Zeeman effect would broaden or split the observed absorption lines. Two measurements of the magnetic field strength in G191–B2B, derived using independent methods give consistent results: Bagnulo & Landstreet (2018) find $B = -280 \pm 965$ G and (Hu et al. 2019) find $B < 2300$ G (3σ upper limit). Using the latter, line shifts due to the quadratic Zeeman effect are $< 10^{-4}$ mÅ, four orders of magnitude below Fe V laboratory wavelength uncertainties. The quadratic Zeeman effect therefore has a negligible impact on measuring $\Delta\alpha/\alpha_0$ (Hu et al. 2019).

7.7 Electric field shifts

G191–B2B has a hydrogen-rich atmosphere (Holberg et al. 1991). Example fundamental stellar parameters are provided by Preval et al. (2013) and Barstow et al. (2003): mass $0.52 M_{\odot}$, radius $0.0204 R_{\odot}$, and surface gravity $GM/R^2 = 3.4 \times 10^5 \text{ m s}^{-2}$. Other measurements include those from Rauch et al. (2013) and Gianninas, Bergeron & Ruiz (2011). At an effective temperature of 52 500 K, a TLUSTY atmospheric synthesis model from Preval et al. (2013) gives a corresponding electron density of $7.0 \times 10^{22} \text{ m}^{-3}$.

Although we may assume overall electrical neutrality, the proton–electron mass difference gives rise to a gravitational separation between the particles in the atmosphere. This separation in turn produces an opposing electric field. Equilibrium between the forces on protons and electrons gives

$$E \approx -\frac{m_p}{2e} \frac{GM}{R^2} \approx -1.8 \times 10^{-2} \text{ V m}^{-1} \quad (6)$$

(Alcock 1980; Koester & Chanmugam 1990). The quadratic electric field shift for atomic transitions is

$$\Delta\omega \sim \frac{-4\pi\epsilon_0 a_0^3 E^2}{\hbar c} \quad (7)$$

(Delone & Krainov 1999) where ω ($=\nu/c$) is the wavenumber (as in equation 2), a_0 is the Bohr radius, ϵ_0 is the permittivity of free space, and \hbar is the reduced Planck constant.

The corresponding shift $\Delta\omega$ is $\sim 10^{-18} \text{ cm}^{-1}$. Using equation (2), approximating $x = 2\Delta\alpha/\alpha_0$ so that $\Delta\alpha/\alpha_0 = \Delta\omega/q$, and using an illustrative $q = 1000$, we obtain $\Delta\alpha/\alpha_0 \sim 10^{-21}$. The

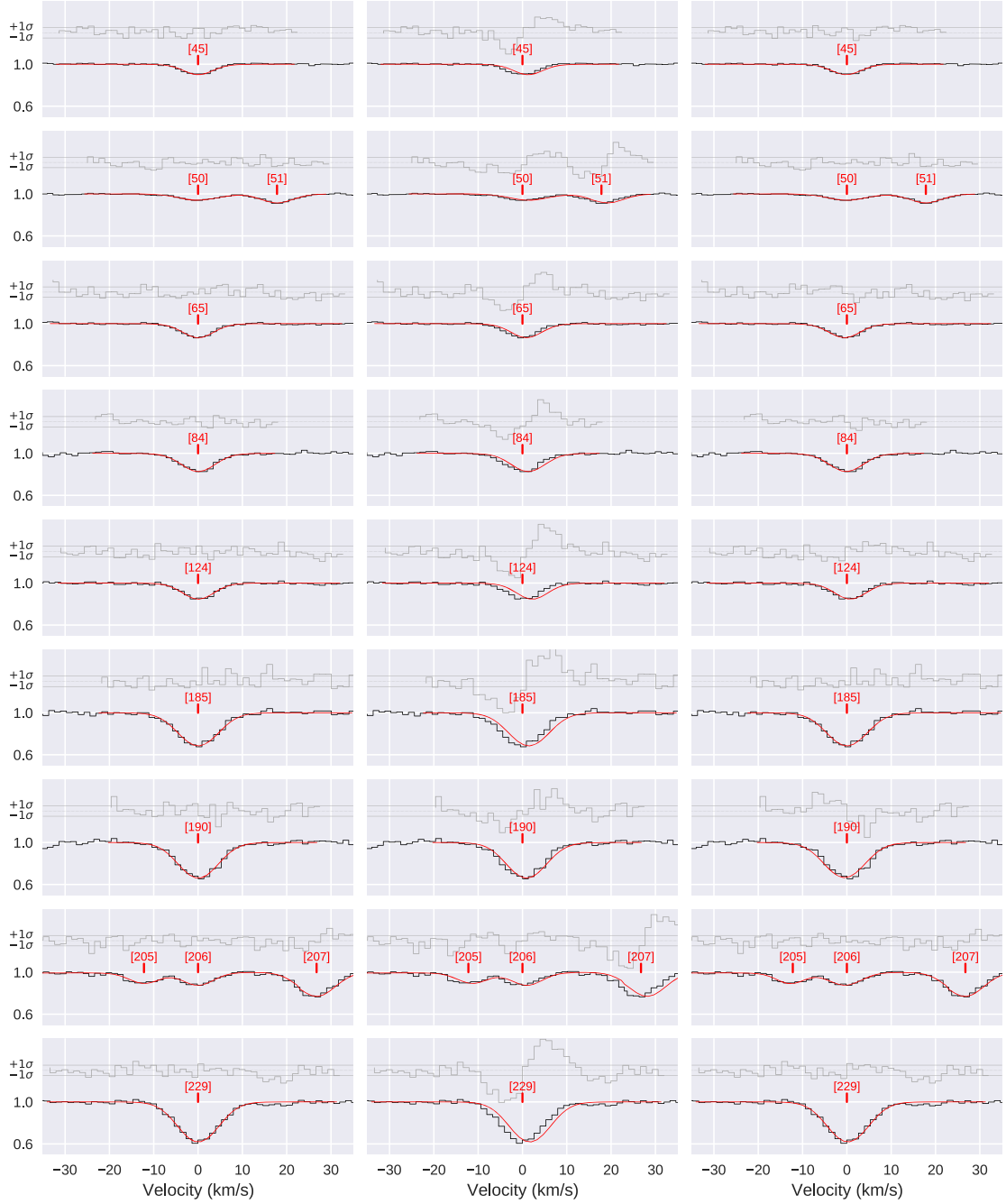


Figure 3. Examples of fits to Fe V lines in the G191–B2B E140 STIS spectrum using vPFIT. The x -axis is wavelength in Å and the y -axis is the normalized flux. The histogram is the data and the Voigt profile fits are overplotted in red. The ticks indicate the line centres with wavelengths and line IDs (see Table 1). Normalized residuals are illustrated above each profile, the horizontal continuous lines indicate 1σ errors. The left-hand column shows the best-fitting model with $\Delta\alpha/\alpha_0$ as a free parameter. The middle column illustrates the exact same model as the left-hand column, but with $\Delta\alpha/\alpha_0$ reset to zero. The right-hand column shows the best-fitting model obtained when $\Delta\alpha/\alpha_0$ is fixed at zero.

electric field shift associated with a static electric field is thus negligible.

8 RESULTS

The final fine-structure constant measurements at the G191–B2B surface, relative to the terrestrial value, are:

$$\Delta\alpha/\alpha_0(K14, 92 \text{ lines}) = (6.36 \pm 0.35_{\text{stat}} \pm 1.84_{\text{sys}}) \times 10^{-5} \quad (8)$$

$$\Delta\alpha/\alpha_0(W19, 53 \text{ lines}) = (4.21 \pm 0.48_{\text{stat}} \pm 2.25_{\text{sys}}) \times 10^{-5} \quad (9)$$

The random and systematic error contributions listed in Table 3, including upper limits, are combined accordingly. The K14 wavelengths produce a result that differs from a null result by 2.9σ whilst the W19 wavelengths indicate a 1.5σ effect. The error contributions are smaller for the K14 sample because of the larger number of Fe V lines in that sample.

Table 3. Summary of actual and potential sources of random (R) and systematic (S) uncertainties and their magnitudes or upper limits. σ_α is the estimated uncertainty on $\Delta\alpha/\alpha_0$ in each case, in units of 10^{-5} . Where two entries appear, the first number corresponds to the results from the K14 Fe v wavelengths, the second from W19.

No.	Uncertainty	σ_α	Type
(1)	Statistical error	0.33, 0.47	R
(2)	Laboratory wavelength errors	1.59(3), 2.00(3)	S
(3)	Long-range distortion	0.1	R
(4)	Photosphere stratification – gravitational redshift effects	$\lesssim 0.1$	S
(5)	Photosphere stratification – bulk velocity flows	≤ 0.1	S
(6)	Fe isotopes – relative abundance variation	≤ 0.05	S
(7)	Zeeman effects	$\leq 10^{-5}$	S
(8)	Electric field shifts	Negligible	S

Clearly, the approaches taken in this paper are very different to the simpler analysis in Berengut et al. (2013), which gives $\Delta\alpha/\alpha_0 = 4.2 \pm 1.6 \times 10^{-5}$, where the uncertainty estimate is derived only from the nominal wavelength uncertainties of the best available Fe v wavelengths at that time (Ekberg 1975). In the present analysis, we have used more recent independent Fe v laboratory measurements, and have explored and quantified a range of potential systematic errors. Our overall uncertainty remains dominated by laboratory wavelength errors, highlighting the need for more advanced calibration methods in laboratory experiments. Despite this, the agreement between all three results is striking.

9 DISCUSSION

In this paper, a comprehensive modelling procedure was applied to measure the fine-structure constant at the surface of the white dwarf G191–B2B, using a single atomic species, Fe v. The *many-multiplet method* (Dzuba et al. 1999a; Webb et al. 1999) has been used to search for any possible change in α in the presence of a gravitational potential 10 000 times the terrestrial value.

Wavelengths of Fe v from two laboratory data sets (Kramida 2014; Ward et al. 2019), with improved uncertainties, were compared against the same transitions observed in the G191–B2B photosphere. Blended, weak, and asymmetric absorption lines have been identified and removed from the sample to try and minimize associated systematic errors.

The overall scatter exhibited in Fig. 1 is in good agreement with the estimated error bars. Nevertheless, Fig. 1 suggests correlated deviations, so some systematic calibration problems may exist in one or both sets of new Fe v wavelengths. In the approximate wavelength range 1290–1360 Å, points lie on average below zero. Whilst the data appears reasonably symmetric about zero above 1350 Å, there is nevertheless a conspicuous clump of high points above ~ 1470 Å.

To advance this field further, several things are required: (i) it is imperative to improve laboratory wavelength precision by at least one order of magnitude, to ~ 0.1 mÅ or preferably much better, (ii) a large sample of white dwarf spectra should be analysed, and (iii) detailed analyses similar to that described in this paper should be carried out on other species such as Fe IV or Ni V.

To summarize, the G191–B2B data calibration/reduction, the Fe v laboratory wavelengths, the q -coefficients, and the methodology used in this paper, are all different to those used in Berengut et al. (2013). Despite this, the consistency between that earlier result and this more

detailed analysis is striking and hints (at the $\sim 3\sigma$ level) that perhaps the fine-structure constant increases slightly in the presence of strong gravitational fields.

ACKNOWLEDGEMENTS

We are most grateful to G. Nave, A. Kramida, and J. Ward for extensive comments on a draft of this paper which lead to many improvements. JKW thanks the John Templeton Foundation, the Department of Applied Mathematics and Theoretical Physics and the Institute of Astronomy at Cambridge University for hospitality and support, and Clare Hall for a Visiting Fellowship during this work. JH is grateful for a CSC Fund and a UNSW scholarship. WULTB wishes to acknowledge support from the French CNRS-PNPS national program. MAB, JDB, MBB, SP, and NR acknowledge the support of the Leverhulme Trust (grant number 2015-278). Finally, we are most grateful to our anonymous referee, who provided many comments that improved the original manuscript.

DATA AVAILABILITY

Based on observations made with the NASA/ESA *HST*, obtained from the data archive at the Space Telescope Science Institute. STScI is operated by the Association of Universities for Research in Astronomy, Inc. under NASA contract NAS 5-26555. The *HST* STIS spectra of G191–B2B are freely available in the Barbara A. Mikulski archive.

REFERENCES

- Aggarwal K., Bogdanovich P., Keenan F., Kisielius R., 2017, *At. Data Nucl. Data Tables*, 114, 1
- Alcock C., 1980, *ApJ*, 242, 710
- Archibald A. M. et al., 2018, *Nature*, 559, 73
- Azarov V. I., Tchchang-Brillet W.-U. L., Wyart J.-F., Launay F., Benharrou M., 2001, *Phys. Scr.*, 63, 438
- Bagnulo S., Landstreet J. D., 2018, *A&A*, 618, A113
- Bainbridge M. et al., 2017a, *Universe*, 3, 32
- Bainbridge M. B. et al., 2017b, in Tremblay P. E., Gaensicke B., Marsh T., eds, *ASP Conf. Ser. Vol. 509, 20th European White Dwarf Workshop*, Astron. Soc. Pac., San Francisco, p. 375
- Barrow J. D., Mota D. F., 2003, *Class. Quantum Gravity*, 20, 2045
- Barrow J. D., Magueijo J. a., Sandvik H. B., 2002, *Phys. Rev. D*, 66, 043515
- Barstow M. A., Hubeny I., Holberg J. B., 1999, *MNRAS*, 307, 884
- Barstow M. A., Good S. A., Holberg J. B., Hubeny I., Bannister N. P., Bruhweiler F. C., Burleigh M. R., Napiwotzki R., 2003, *MNRAS*, 341, 870
- Barstow M. A., Barstow J. K., Casewell S. L., Holberg J. B., Hubeny I., 2014, *MNRAS*, 440, 1607
- Bekenstein J. D., 1982, *Phys. Rev. D*, 25, 1527
- Berengut J. C., Flambaum V. V., Ong A., Webb J. K., Barrow J. D., Barstow M. A., Preval S. P., Holberg J. B., 2013, *Phys. Rev. Lett.*, 111, 010801
- Bergeron P., Saffer R. A., Liebert J., 1992, *ApJ*, 394, 228
- Carswell R. F., Webb J. K., 2020a, <https://people.ast.cam.ac.uk/~rfc/>
- Carswell R. F., Webb J. K., 2020b, <https://www.overleaf.com/read/vbxcfnfgksr>
- Carswell R. F., Webb J. K., Cooke A. J., Irwin M. J., 2014, *Astrophysics Source Code Library*, record ascl:1408.017, <https://www.ast.cam.ac.uk/rfc/vpfit.html>
- Carvalho G. A., Marinho R. M., Malheiro M., 2018, *General Relativ. Gravit.*, 50, 38
- Chayer P., Fontaine G., Wesemael F., 1995, *ApJS*, 99, 189
- Delone N. B., Krainov V. P., 1999, *Phys.-Uspe.*, 42, 669
- Dicke R. H., 1959, *Science*, 129, 621

- Dicke R. H., 1964, *The Theoretical Significance of Experimental Relativity*. Gordon & Breach, New York
- Dicke R. H., 2019, *General Relativ. Gravit.*, 51, 57
- Dreizler S., Wolff B., 1999, *A&A*, 348, 189
- Dumont V., Webb J. K., 2017, *MNRAS*, 468, 1568
- Dzuba V. A., 2005, *Phys. Rev. A*, 71, 032512
- Dzuba V. A., Johnson W. R., 1998, *Phys. Rev. A*, 57, 2459
- Dzuba V. A., Flambaum V. V., Kozlov M. G., 1996, *Phys. Rev. A*, 54, 3948
- Dzuba V. A., Flambaum V. V., Webb J. K., 1999a, *Phys. Rev. A*, 59, 230
- Dzuba V. A., Flambaum V. V., Webb J. K., 1999b, *Phys. Rev. Lett.*, 82, 888
- Dzuba V. A., Flambaum V. V., Marchenko M. V., 2003, *Phys. Rev. A*, 68, 022506
- Ekberg J. O., 1975, *Phys. Scr.*, 12, 42
- Fawcett B. C., Henrichs H. F., 1974, *A&AS*, 18, 157
- Flambaum V. V., Dzuba V. A., 2009, *Can. J. Phys.*, 87, 25
- Flambaum V. V., Shuryak E. V., 2008, in Danilewicz P., Piecuch P., Zelevinsky V., eds, *AIP Conf. Ser. Vol. 995, Nuclei and Mesoscopic Physic – WNMP 2007*, AIP. p. 1, preprint ([astro-ph/0701220](https://arxiv.org/abs/astro-ph/0701220))
- Fontaine G., Brassard P., Charpinet S., Randall S. K., Van Grootel V., 2013, in Shibahashi H., Lynas-Gray A. E., eds, *ASP Conf. Ser. Vol. 479, Progress in Physics of the Sun and Stars: A New Era in Helio- and Asteroseismology*, Astron. Soc. Pac., San Francisco, p. 211
- Gianninas A., Bergeron P., Ruiz M. T., 2011, *ApJ*, 743, 138
- Hees A. et al., 2020, *Phys. Rev. Lett.*, 124, 081101
- Holberg J. B., Ali B., Carone T. E., Polidan R. S., 1991, *ApJ*, 375, 716
- Holberg J. B., Hubeny I., Barstow M. A., Lanz T., Sion E. M., Tweedy R. W., 1994, *ApJ*, 425, L105
- Hu J. et al., 2019, *MNRAS*, 485, 5050
- Hubeny I., Lanz T., 1995, *ApJ*, 439, 875
- Hubeny I., Lanz T., 2011, *Astrophysics Source Code Library*, record ascl:1109.022
- Jain R. K., Kouvaris C., Nielsen N. G., 2016, *Phys. Rev. Lett.*, 116, 151103
- Johnson W. R., Sapirstein J., 1986, *Phys. Rev. Lett.*, 57, 1126
- Kalinin S. K. et al., 1985, *Acad. Sci. Kazakh. SSR, Alma-Ata, USSR*
- King J. A., Mortlock D. J., Webb J. K., Murphy M. T., 2009, *Mem. Soc. Astron. Italiana*, 80, 864
- Koester D., Chanmugam G., 1990, *Rep. Prog. Phys.*, 53, 837
- Kramida A., 2011, *Comput. Phys. Commun.*, 182, 419
- Kramida A., 2013, *Fusion Sci. Technol.*, 63, 313
- Kramida A., 2014, *ApJS*, 212, 11
- Magueijo J., Barrow J. D., Sandvik H. B., 2002, *Phys. Lett. B*, 549, 284
- Mota D. F., Barrow J. D., 2004a, *MNRAS*, 349, 291
- Mota D. F., Barrow J. D., 2004b, *Phys. Lett. B*, 581, 141
- Ong A., Berengut J. C., Flambaum V. V., 2013, *Phys. Rev. A*, 88, 052517
- Preval S. P., Barstow M. A., Holberg J. B., Dickinson N. J., 2013, *MNRAS*, 436, 659
- Rauch T., Werner K., Bohlin R., Kruk J. W., 2013, *A&A*, 560, A106
- Sion E. M., Greenstein J. L., Landstreet J. D., Liebert J., Shipman H. L., Wegner G. A., 1983, *ApJ*, 269, 253
- Sion E. M., Bohlin R. C., Tweedy R. W., Vauclair G. P., 1992, *ApJ*, 391, L29
- Uzan J.-P., 2011, *Living Rev. Relativ.*, 14, 2
- Voisin G., Cognard I., Freire P. C. C., Wex N., Guillemot L., Desvignes G., Kramer M., Theureau G., 2020, *A&A*, 638, A24
- Ward J., Nave G., 2015a, in *IAU General Assembly, Vol. 22*, p. 2253006
- Ward J. W., Nave G., 2015b, in *American Astronomical Society Meeting Abstracts #225*. p. 339.03
- Ward J. W., Raassen A. J. J., Kramida A., Nave G., 2019, *ApJS*, 245, 22
- Webb J. K., Flambaum V. V., Churchill C. W., Drinkwater M. J., Barrow J. D., 1999, *Phys. Rev. Lett.*, 82, 884
- Werner K., Dreizler S., 1994, *A&A*, 286, L31
- Wheeler J. C., Hansen C. J., Cox J. P., 1968, *Astrophys. Lett.*, 2, 253
- Zuckerman B., Koester D., Reid I. N., Hünsch M., 2003, *ApJ*, 596, 477

SUPPORTING INFORMATION

Supplementary data are available at [MNRAS](https://www.mnras.org/) online.

Table S1. Atomic data used. **K14** are Ritz wavelengths (Kramida 2014).

Table S2. Observed line wavelengths in the STIS spectrum of G191–B2B. ID refers to the number in column 1 of Table 1.

Please note: Oxford University Press is not responsible for the content or functionality of any supporting materials supplied by the authors. Any queries (other than missing material) should be directed to the corresponding author for the article.

This paper has been typeset from a $\text{\TeX}/\text{\LaTeX}$ file prepared by the author.